Control Surface Allocation Based on Offline Handling Quality Simulations for a Flying Wing Aircraft

Asaro, S.; Atmaca, D.; van Kampen, E.; Vos, Roelof

DOI
10.2514/6.2025-2475

Publication date
2025

Document Version
Final published version

Published in
Proceedings of the AIAA SCITECH 2025 Forum

AIAA SciTech Forum
6-10 January 2025, Orlando, FL
AIAA SCITECH 2025 Forum

10.2514/6.2025-2475

Control Surface Allocation based on Offline Handling Quality Simulations for a Flying Wing Aircraft

Salvatore Asaro*, Direnc Atmaca†, Erik-Jan van Kampen‡, Roelof Vos§
Delft University of Technology, Kluyverweg 1 2629HS, Delft, The Netherlands

Commercial applications of flying wing aircraft, as the Flying-V here considered, can contribute to reducing carbon and nitrogen emissions produced by the aviation sector. However, because of the lack of a tail, all flying wing aircraft have reduced controllability. For this reason, the placement and sizing of the control surfaces along the wing is a non-trivial problem. The paper focuses on solving this problem using offline handling quality simulations based on certification requirements. In different flight conditions, the aircraft must be able to perform a certain set of maneuvers as defined by the certifying authorities. First, offline simulations calculate the minimum control authority required from the elevator, aileron, and rudder to perform each maneuver. Then, based on the global minimum for all maneuvers, the control surfaces are sized and placed along the wings. The aerodynamic model employed uses a combination of Reynolds-averaged Navier-Stokes (RANS) and vortex lattice method (VLM) simulations. The control authority of the control surfaces is estimated with VLM and VLM calibrated with RANS simulations, showing significant differences between the two.

Nomenclature

A_x, A_y, A_z	acceleration along X, Y, Z axis, m/s^2	U_∞	freestream velocity, m/s
b	wing span, m	X	axis and coordinate along chord direction, m
$\overline{c}$	mean aerodynamic chord, m	x_{hinge}	hinge line
CG	center of gravity, m	Y	axis and coordinate along span direction, m
C_x, C_y, C_z	force coefficient along X, Y, Z	Z	axis and coordinate along vertical direction, m
C_{m_x}, C_{m_y}, C_{m_z}	moment coefficient around X, Y, Z	α	angle of attack, °
g	gravitational acceleration, m/s^2	β	sideslip angle, °
h	altitude, m	δ_a, δ_e, δ_r	aileron, elevator, rudder deflection angle, °
H	transfer function	$\dot{\delta}$	control surface deflection rate, °/s
I	moment of inertia, kg·m^2	ρ_∞	freestream density, kg/m^3
J	cost function	ϕ	bank angle, °
K	gain	θ	pitch angle, °
m	aircraft mass, kg	ζ	damping ratio
M_∞	freestream Mach number	ω	natural frequency, rad/s
p, q r	angular velocity around X, Y, Z, rad/s	act	actuator
$\hat{p}$, $\hat{q}$, $\hat{r}$	dimensionless p, q r	eng	engine
$\dot{p}$, $\dot{q}$ $\dot{r}$	angular acceleration around X, Y, Z rad/s^2	MTOW	Maximum take-off weight, N
$Re_{\overline{c}}$	mean chord Reynolds number	MLW	Maximum landing weight, N
s	Laplace variable (for continuous-time systems)	RANS	Reynolds-averaged Navier-Stokes
		VLM	Vortex lattice method
T	thrust, N		

*Postdoctoral Researcher, Faculty of Aerospace Engineering, s.asaro@tudelft.nl
†PhD Candidate, Faculty of Aerospace Engineering, d.atmaca@tudelft.nl, AIAA Student Member
‡Associate Professor, Faculty of Aerospace Engineering, e.vankampen@tudelft.nl
§Associate Professor, Faculty of Aerospace Engineering, R.Vos@tudelft.nl, AIAA Associate Fellow

I. Introduction

The Flightpath 2050 report issued by the Advisory Council for Aeronautics Research in Europe (ACARE) sets an ambitious goal of reducing greenhouse gas emissions [1]. Particularly, a reduction of 75% for CO_2 and 90% for NO_x are defined as targets with respect to conventional aircraft from 2000. Novel aircraft designs, such as flying wing aircraft, could reduce drag, contributing to reducing the aviation sector's footprint. Several flying wing designs are being investigated [2], most of them feature highly swept inner wings to replace the fuselage, such as the Flying-V [3]. An artist's impression of the Flying-V is depicted in Figure 1a and a top view with the cabin layout in Figure 1b. The airplane has an inner wing with a sweep angle of ca. 64° and an outer wing with a sweep angle of ca. 39°. The wing span is b = 63 m, and the mean aerodynamic chord $\overline{c}$ = 18 m. The current design without engines shows a maximum lift-to-drag ratio of 24.2 under cruise conditions, with angle of attack α = 3.6° and freestream Mach number M_∞ = 0.85 [4].

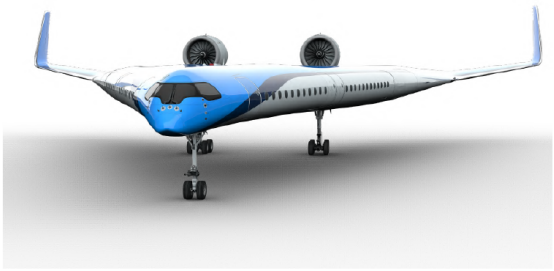

(a) Artistic impression

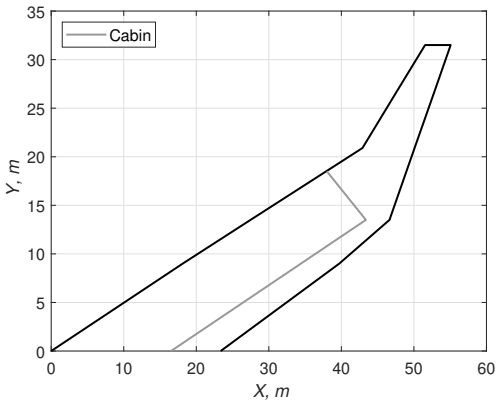

(b) Top view

Fig. 1 Artistic impression and top view of Flying-V aircraft

The initial design of the airplane features control surfaces along the trailing edge of the outer wing that act as both an elevator and an aileron for pitch and roll control, respectively. The yaw is controlled with rudders spanning the height of the winglets. The current design of the control surfaces has been tested in a simulator [5], in which the aerodynamic model used to describe the aircraft relies on vortex lattice method simulations. Various maneuvers are tested in the simulator to study longitudinal and lateral-directional behavior. Longitudinal maneuvers are mainly pitch and flight path angle tracking and capture tasks, where the desired performance is set using a scoring algorithm. On the other hand, lateral-directional maneuvers focus on the bank-to-bank, coordinated turn, and steady heading sideslip requirements outlined by EASA CS-25 [6]. In addition, the simulator tests look at the Dutch roll response of the aircraft. For this, pilots are asked to give a doublet rudder input once the aircraft is in a sustained oscillation to counteract this by any means possible. The tests indicate that the Dutch roll is unstable and difficult to suppress with the control authority available to the pilots. Furthermore, the limited control authority of the rudders is also evident from the steady-heading sideslip maneuver where the aircraft fails to follow any desired sideslip angle $\beta > 5°$. In addition, some slight pitch dropout is observed during the bank-to-bank maneuver due to elevator saturation. Most longitudinal results are between level 1 and level 2 based on Cooper-Harper ratings translated into the military handling quality scale between 1 and 3. Overall, the simulation tests show that the design of control surfaces should be improved to meet all certification requirements.

The maneuvers tested in the flight simulator can be simulated offline, allowing the testing of new control surface layouts with low computational efforts. Previous studies have sized the control surfaces similarly based on offline handling quality simulations in unconventional aircraft [7]-[8]. A similar approach is also pursued here, with an aerodynamic model of the aircraft which incorporates RANS simulations and hence possible nonlinear effects in the early phase of the aircraft design [9].

The contribution of this paper is to size, place, and define the control surface required for a novel flying-wing aircraft such as the Flying-V. The control surface layout is driven by the maneuvers that an aircraft must be able to perform inside its flight envelope. The maneuvers are defined by handling quality requirements, and compliance is demonstrated

through offline simulations. The aerodynamic model of the Flying-V is introduced in Section II.A, together with the flight conditions considered. The maneuvers tested are presented in Section II.E. For each maneuver, the required control authority of the elevator, the aileron, and the rudder are estimated, and then the control surfaces are sized and placed on the wing accordingly. Their combination will define the final control surface layout for the Flying-V aircraft.

II. Methodology

The control surfaces are sized according to the maneuvers described in Section II.E. The maneuvers are simulated in a framework in which the aerodynamic model (Section II.A) is converted into the rigid body dynamics of the aircraft (Section II.B). For each maneuver, simulations are run iteratively to identify a range of control surface derivatives that can satisfy its requirements. The minimum control surface derivative is then selected as the sizing case and is used to find a control surface of the aircraft that can provide the requested control surface derivative. The same process is then repeated for all the selected maneuvers, leading to the new control surface layout.

A. Aerodynamic model

The parameters influencing forces and moments are determined with a combination of Reynolds-averaged Navier–Stokes (RANS) and Vortex Lattice Method (VLM) simulations; further details on the aerodynamic model can be found in [9]. A summary of the parameters that influence the forces and moments acting on the aircraft is presented in Table 1, which also indicates if the parameter is determined with RANS (r) or VLM (v). The variables in the table are α the angle of attack, β the sideslip angle, δ_{e}, δ_{a}, δ_{r}, δ_{hl} the deflection of the elevator, aileron, rudder and high lift device, and the dimensionless angular rates $\hat{p} = pb/(2U_\infty)$, $\hat{q} = q\bar{c}/(2U_\infty)$ and $\hat{r} = rb/(2U_\infty)$, where p, q and r are the angular rates corresponding to the X, Y and Z axes, respectively.

Table 1 Force and moment coefficient dependencies, marked r when determined with RANS simulations and v with VLM simulations

	α	$\beta(\alpha)$	$\hat{p}$	$\hat{q}$	$\hat{r}$	$\delta_e(\alpha)$	$\delta_a(\alpha)$	$\delta_r(\alpha)$	$\delta_{hl}(\alpha)$
C_X	r					v - r	v - r	v - r	v - r
C_Y		r			v		v - r	v - r	v - r
C_Z	r			v		v - r			v - r
C_{m_x}		r	v		v		v - r	v - r	
C_{m_y}	r			v		v - r			v - r
C_{m_z}		r	v		v		v - r	v - r	

The RANS simulations determine the forces and moments generated by a single control surface design for the aileron, elevator, high-lift device, and rudder. The results are then used to calibrate the VLM simulations, which are less time-consuming. For this reason, the results presented in Section III, are divided into VLM and VLM calibrated with RANS. Further details on the control surfaces simulated with RANS are introduced in [9].

The maneuvers are tested at several flight conditions, summarized in Table 2. The selected operating conditions are chosen to represent different phases of the flight envelope. The different conditions are divided into two groups, i.e., MLW (Maximum Landing Weight) with m_{MLW} = 202 10^3 kg and MTOW (Maximum Take-off Weight) with m_{MTOW} = 266 10^3 kg. The masses are derived from [10], assuming a family-optimized Flying V-1000 aircraft.

Three different types of control surfaces are considered: elevator, aileron and rudder. Table 3, based on [11] indicates their maximum and minimum deflection angles and maximum deflection rates. The indicated limits are used during the simulations; however, new maximum and minimum deflections are suggested in Section III to satisfy specific requirements when required.

B. Rigid body dynamics

By expressing the aerodynamic force and moment coefficients in the body frame, it is possible to convert them into linear and rotational accelerations. The system of equations is derived based on the following assumptions: 1) the aircraft is rigid and with a constant mass m, 2) the Earth is flat and non-rotating, 3) the gravitational acceleration g is constant, 4) the aircraft has a plane of symmetry in the body-fixed frame such that $I_{xy} = I_{yz} = 0$, 5) the resultant thrust

Table 2 Flight conditions

	h, m	ρ_∞, kg/m^3	U_∞, m/s	M_∞	Re_c (10^7)	m (10^3), kg
MLW	0	1.22	68.6	0.2	8.4	202
	0	1.22	85.1	0.25	10.5	202
	0	1.22	102.1	0.3	12.6	202
MTOW	0	1.22	102.1	0.3	12.6	266
	5450	0.70	127.5	0.4	10	266
	7650	0.55	185.7	0.6	11.9	266
	9750	0.43	210.4	0.7	11	266
	11225	0.35	250.8	0.85	7.1	266

Table 3 Control surfaces characteristics

	δ, °	$\dot{\delta}$, °/s
Elevator	± 25	40
Aileron	± 25	55
Rudder	± 25	50

vector is on the symmetry plane and hence only affects the force on X and Z and M_y. Based on these assumptions, the system of equations is expressed as:

$$
\begin{aligned}
A_x &= \frac{C_X}{m} - g\sin\theta \\
A_y &= \frac{C_Y}{m} + g\sin\phi\cos\theta \\
A_z &= \frac{C_Z}{m} + g\cos\theta\cos\phi \\
\dot{p} &= \frac{I_{zz}}{I^*}C_{m_x} + \frac{I_{xz}}{I^*}C_{m_z} + \frac{\left(I_{xx} - I_{yy} + I_{zz}\right)I_{xz}}{I^*}pq + \frac{\left((I_{yy} - I_{zz})I_{zz} - I_{xz}^2\right)}{I^*}qr \\
\dot{q} &= \frac{C_{m_y}}{I_{yy}} + \frac{I_{xz}(r^2 - p^2)}{I_{yy}} + \frac{I_{zz} - I_{xx}}{I_{yy}}pr \\
\dot{r} &= \frac{I_{xz}}{I^*}C_{m_x} + \frac{I_{xx}}{I^*}C_{m_z} + \frac{\left(-I_{xx} + I_{yy} - I_{zz}\right)I_{xz}}{I^*}qr + \frac{\left((I_{xx} - I_{yy})I_{xx} + I_{xz}^2\right)}{I^*}pq
\end{aligned}
\tag{1}
$$

where $I^* = I_{xx}I_{zz} - I_{xz}^2$. All linear and angular body velocities can be obtained by integrating these equations. In addition, the kinematic equations that allow converting body velocities into Euler angles can be expressed as

$$
\begin{aligned}
\dot{\phi} &= p + q\sin\phi\tan\theta + r\cos\phi\tan\theta \\
\dot{\theta} &= q\cos\phi - r\sin\phi \\
\dot{\psi} &= q\frac{\sin\phi}{\cos\theta} + r\frac{\cos\phi}{\cos\theta}
\end{aligned}
\tag{2}
$$

C. Actuator and Engine Dynamics

The actuators (act) are modeled as a second-order system based on [12], and the engines (eng) are modeled as a first order system. Their transfer functions are as follows:

$$
H_{\text{act}}(s) = \frac{4000}{s^2 + 140s + 4000} = \frac{\omega_n^2}{s^2 + 2\zeta\omega_n + \omega_n^2} \quad \text{and} \quad H_{\text{eng}}(s) = \frac{1}{0.2s + 1} \tag{3}
$$

For the actuators, this leads to a natural frequency $\omega_n = 63.246$ rad/s and a damping ratio $\zeta = 1.107$.

D. Simulation model

The simulation model encapsulates the aerodynamic model, the rigid body dynamics, and the control law used to command the aircraft. Figure 2 shows the layout of the simulation model.

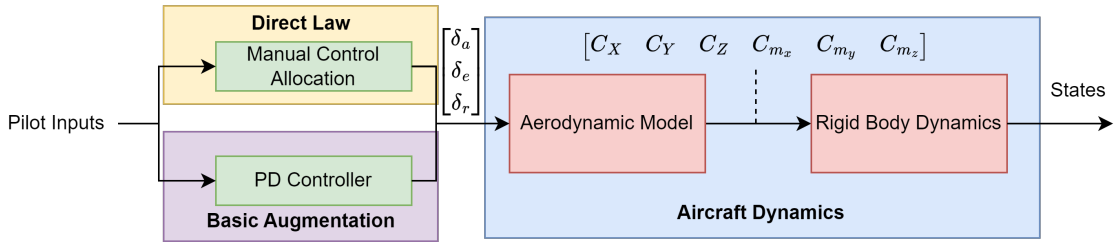

Fig. 2 Model structure for offline simulations

Based on the figure, two types of control laws act as bridges between the pilot commands and control surface deflections. In direct law, pilot inputs are manually mapped over the control surfaces such that the sidestick and pedal inputs the pilot gives directly command the control surfaces. This would be sufficient to study the aircraft's handling qualities in a real-time simulation environment. However, a simple controller replaces the pilot since simulations are conducted offline. It is designed to have a basic proportional-derivative structure to ensure the controller does not mask any natural characteristic of the airframe.

The control deflections computed through either direct law or basic augmentation serve as inputs to the aerodynamic model to calculate the forces and moments acting on the aircraft. These are then used in dynamical equations given in Equation 1. The final states of the aircraft are calculated by integrating the linear and rotational accelerations of the aircraft, and using the kinematic transformations given in Equation 2. The structure of the PD controller is shown in Figure 3.

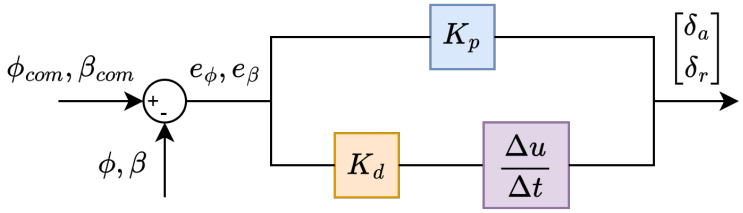

Fig. 3 Proportional-derivative controller used in basic augmentation

When the controller is active, it is applied only to the roll and sideslip channels. Several maneuvers in this study require the aircraft to reach and maintain a specific sideslip and/or bank angle. The pitch channel uses the direct law in all cases. The gains of the controller are obtained by trial and error, separately for roll and sideslip, where $K_{p_\beta} = K_{d_\beta} = K_{p_\phi} = 5000$ with $K_{d_\phi} = 1000$. The trial-and-error process aims to find a fast control response without excessive overshoot. Although the gains might seem high at first glance, this is because sideslip and beta are defined in radians, whereas the aileron and rudder deflections are in degrees.

For the sizing maneuvers explained in the following section, the controller is active for steady heading sideslip, one-engine-out, bank-to-bank, and coordinated turn. The longitudinal trim condition is calculated statically using a cost function and minimization algorithm. The direct law is used without any control augmentation to test the calculated trim point in a steady-level flight scenario. The aim of the cost function and the minimization algorithm is to find a steady state for the aircraft such that the longitudinal acceleration terms, $\dot{u}$, $\dot{w}$, $\dot{q}$ and the flight path angle γ are zero. In addition, the cost function seeks to minimize the difference between the desired airspeed (V_{des}) and the trim airspeed (V_{trim}). This cost function is given in Equation 4.

$$J(\dot{u}, \dot{w}, \dot{q}, \dot{V}, \dot{\gamma}) = 100 \cdot \dot{u}^2 + 1 \cdot \dot{w}^2 + 100 \cdot \dot{q}^2 + 100 \cdot (V_{des} - V_{trim})^2 + 100 \cdot \gamma^2 \tag{4}$$

The variables of this cost function can all be expressed in terms of aerodynamic forces and moments using Equation 1. Hence, the problem of minimizing the accelerations indirectly becomes a net force/moment minimization problem.

Given that longitudinal forces and moments are related to elevator deflection δ_e, angle of attack α, and engine thrust T, the minimization algorithm tries to iteratively change these parameters to find the global minimum of the cost function.

In a recent simulator flight test conducted on an aerodynamic model of the Flying-V, which relied only on VLM simulations, the Dutch roll is found to be unstable [5]. Consequently, this is a point of concern for the new aerodynamic model used in this study. For this reason, as a pre-check before running the actual sizing simulations, an offline Dutch roll simulation is conducted for all flight conditions using the direct law. Control augmentation for the Dutch roll is avoided to prevent masking the fundamental structural response of the aircraft. To this end, the nonlinear simulation model is excited using a doublet rudder input and then allowed to evolve without interference to observe whether the sideslip oscillations dampen out over time. Figure 4a shows the time histories of the sideslip angles for some flight conditions. The overall trend is that the oscillations are observed to damp out, and the frequency increases with M_∞.

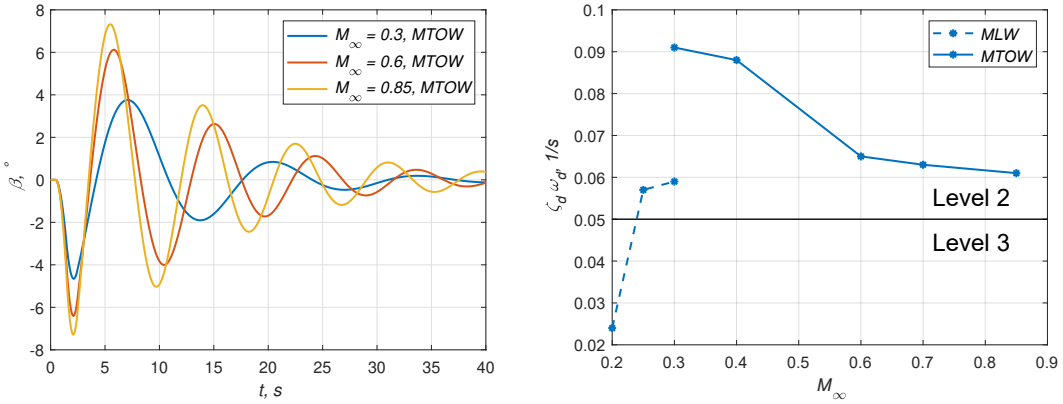

(a) Dutch simulation results in some flight conditions

(b) Damping-frequency product

Fig. 4 Dutch roll simulation results and damping-frequency product

To analyze these time histories in more detail, the logarithmic decrement method is used to calculate the natural frequency and damping ratio of the oscillations, which are given as the following:

$$\zeta_d = \frac{1}{n} log\left(\sum_{k=0}^{n} \frac{x(t_k)}{x(t_{k+1})}\right) \tag{5}$$

$$T_{avg} = \frac{1}{n}\left(\sum_{k=0}^{n} t_{k+1} - t_k\right), \qquad \omega_d = 2\pi T_{avg} \tag{6}$$

where n is the number of peaks, x is the amplitude of the peaks, and t_k is the time of the peaks. Hence, the damping ratio is calculated by taking the sum of consecutive peaks and averaging them, whereas the frequency comes from averaging the consecutive periods of oscillation. The final values of ζ_d and ω_d determine the handling qualities based on the MIL-STD-1797A standards [13]. Assuming that the Flying-V model falls under class III aircraft, the classifications in Table 4 are obtained for the terminal and nonterminal flight phases.

Table 4 Dutch roll classifications based on MIL-STD-1797A

	Category C - Terminal Flight Phases			Category B - Nonterminal Flight Phases		
	ω_d, rad/s	ζ_d	$\zeta_d\omega_d$, rad/s	ω_d, rad/s	ζ_d	$\zeta_d\omega_d$, rad/s
Level 1	≥ 0.4	≥ 0.08	≥ 0.10	≥ 0.4	≥ 0.08	≥ 0.15
Level 2	≥ 0.4	≥ 0.02	≥ 0.05	≥ 0.4	≥ 0.02	≥ 0.05
Level 3	≥ 0.4	≥ 0	-	≥ 0.4	≥ 0	-

Using Equations 5 and 6, comparing the results with the Dutch roll requirements reveals that the Dutch roll is stable and damped under all flight conditions. These results are given in Table 5 and Figure 4b. The figure only depicts the

damping-frequency product, as this criterion serves as the primary driving factor for the HQ classifications in this application. From these, the Dutch roll in almost all flight conditions is within Level 2, which indicates that although its damping is not strong, it is stable.

An important point to mention is that these Dutch roll classifications are mainly used for linearized aircraft models. However, one could argue that using a nonlinear simulation model is more accurate and allows for the possibility of revealing undesired phenomena. Nevertheless, due to the nonlinear nature of the model, the handling quality ratings for the Dutch roll serve as an approximation.

Table 5 Dutch roll analysis and classification results

Flight Conditions	Flight Phase	ω_d, rad/s	ζ_d	$\zeta_d\omega_d$, rad/s	HQ Level
M = 0.2 (MLW)	Terminal	0.389	0.062	0.0024	< 3
M = 0.25 (MLW)	Terminal	0.436	0.130	0.057	2
M = 0.3 (MLW)	Terminal	0.446	0.133	0.059	2
M = 0.3 (MTOW)	Nonterminal	0.465	0.196	0.091	2
M = 0.4 (MTOW)	Nonterminal	0.433	0.203	0.088	2
M = 0.6 (MTOW)	Nonterminal	0.670	0.097	0.065	2
M = 0.7 (MTOW)	Nonterminal	0.586	0.108	0.063	2
M = 0.85 (MTOW)	Nonterminal	0.731	0.083	0.061	2

E. Criteria for Sizing Control Surfaces

The aileron, the elevator, and the rudder control the moment around the x, y, and z axis, respectively. A series of criteria are defined in the certification documentation that allows sizing of the control surface required for each function. In this work, each control surface is supposed to carry a dedicated task. For example, the aileron is not used for elevator purposes. This approach is preferred for two main reasons: it allows for the clear division of the actuators, which require a faster deflection rate, such as the aileron, and hence lower inertia of the control surface and higher power. The second reason is to be conservative; i.e., the main interest of this work is to determine which part and how much of the wing area is required to implement the necessary control surfaces. In a second phase, the elevator or part of it could be employed as an aileron and vice versa, leading to lower control surface deflection required and, hence, to lighter actuator systems.

The control surfaces are sized for the flight conditions listed in Table 2 for the most forward CG location. Herein, the functions used to size the different control surfaces are summarized:

1. Elevator

- *Longitudinal trim*: the elevator is sized to longitudinally trim the aircraft. The elevator is placed on the outer wing as inboard as possible to allow enough space to allocate the aileron. The longitudinal trim procedure also allows determining the required angle of attack α and thrust T at a certain flight condition. The identified longitudinal trim condition is then used as the starting point for the remaining cases. Furthermore, the thrust lapse with the operating conditions is estimated for the engine considered in this work, for which $T/W = 0.27$ at take-off. A detailed engine description can be found in [14]. The thrust is assumed to scale with the Mach number and the altitude according to [15]:

$$T = T_{\max}\frac{p_{t,\infty}}{p_0}\left[1 - (0.43 + 0.014 \cdot \mathrm{BPR})\sqrt{M_\infty}\right] \tag{7}$$

  where $p_{t,\infty}$ is the freestream total pressure, p_0 the sea level pressure of 101 kPa. For the operating conditions considered in this paper, $\frac{T_{t,\infty}}{T_0}$ is always lower than 1.06, hence Eq. 7 is sufficient to describe the thrust lapse. The total pressure and temperature are calculated with the isentropic equations. The thrust lapse obtained for the engine here considered is depicted in Figure 6b.

2. Rudder

- *Steady heading sideslip*: the aircraft should keep a constant heading while facing a certain sideslip angle β. This maneuver assesses the capabilities of the aircraft during crosswind. The certification documentation EASA CS-25

(AMC 25.177(c)) [6] defines $\beta = \text{asin}(30/U_\infty)$, where the velocity is expressed as calibrated airspeed in knots. The sideslip values are listed in Table 6 for the flight conditions considered here.

Table 6 Sideslip angle β at the considered flight conditions

	MLW			MTOW				
M_∞	0.2	0.25	0.3	0.3	0.4	0.6	0.7	0.85
β	13.10°	10.45°	8.69°	8.69°	8.86°	6.97°	6.85°	6.17°

- *one engine inoperative*: a second function of the rudder is to compensate the C_{m_z} induced by one engine when the other fails. Although the location of the engines is still under investigation [14], it is assumed to be located at $Y = 5.7$ m, $Z = 0$ m.

3. Aileron

- *Bank-to-bank*: the aircraft is required to bank from -30° to 30° in 7 s or less. During the maneuver, the flight path should be kept between 0° and 5°.

Additionally, the aileron is also used to compensate for the effect induced by the rudder and prevent the aircraft from rolling during one-engine out and steady-heading sideslip maneuvers.

F. Verification of sizing - Coordinated turn

After sizing the control surfaces, a coordinated turn is considered to combine longitudinal and lateral-directional motions. This maneuver allows testing the combination of the three control surfaces, i.e., studying the aircraft's capability to coordinate yaw, pitch, and roll simultaneously. A turn is performed at a constant speed, minimizing the sideslip angle. The requirement is to perform the maneuver for 10 s while keeping the bank angle between 40° and 45° and the flight path angle between 0° and 5°.

III. Results

Section III.A introduces how the sizing is conducted with the example of the elevator sizing, and summarizes the conditions required for longitudinal trim. Section III.B deals with the sizing of high lift devices and why they are needed at low speed. Section III.C presents the aileron and rudder needed to satisfy the certification documentation requirements. Finally, in Section II.F, the newly defined control surfaces are tested with the coordinated turn.

A. Sizing of Elevator

At first, the elevator is sized to find longitudinal trim conditions, such as, for example, the angle of attack α and the required thrust T, which are then employed as a starting point to perform the other maneuvers to size the aileron and the rudder. Figure 5a shows the discretization of the outer wing trailing edge area used to test different elevator designs. The considered area is discretized into nine sections along the span and four along the chord. For elevator sizing, the most inboard sections are first considered to leave the outer sections to place the aileron. For example, the first elevator considered is the most inboard panel with the hinge line closer to the trailing edge, $x_{hinge}/c = 0.95$. After that, the hinge line is moved upstream, up to $x_{hinge}/c = 0.65$. The control authority of the four different described elevators is shown in Figure 5b as the blue line closer to zero for $C_{m_{y,\delta_e}}$. The same procedure is then applied when increasing the number of panels along the span, with the simplification that the hinge line is fixed, to avoid steps in the control surface or "hollowed" control surfaces. Figure 5b shows the control authorities of the considered elevator, which are 48 in total.

The black horizontal line in the figure indicates the minimum requirement to satisfy the longitudinal trim conditions. This requirement is determined in the different flight conditions introduced in Table 2, with a maximum possible deflection of 25° as presented in Table 3. The minimum requirement is determined by running ten simulations introduced in Section II.D and selecting the smaller control authority which can satisfy the deflection angle constrain. A similar procedure is then repeated with the other control surfaces for the selected maneuvers.

The output of the longitudinal trim simulations is the angle of attack α and the thrust T as depicted in Figures 6a and 6b, respectively. The thrust is shown as the thrust-to-weight ratio, where the weight is the maximum take-off weight (MTOW). T is required thrust for level flight, i.e., to compensate the component of the weight and the force along the X

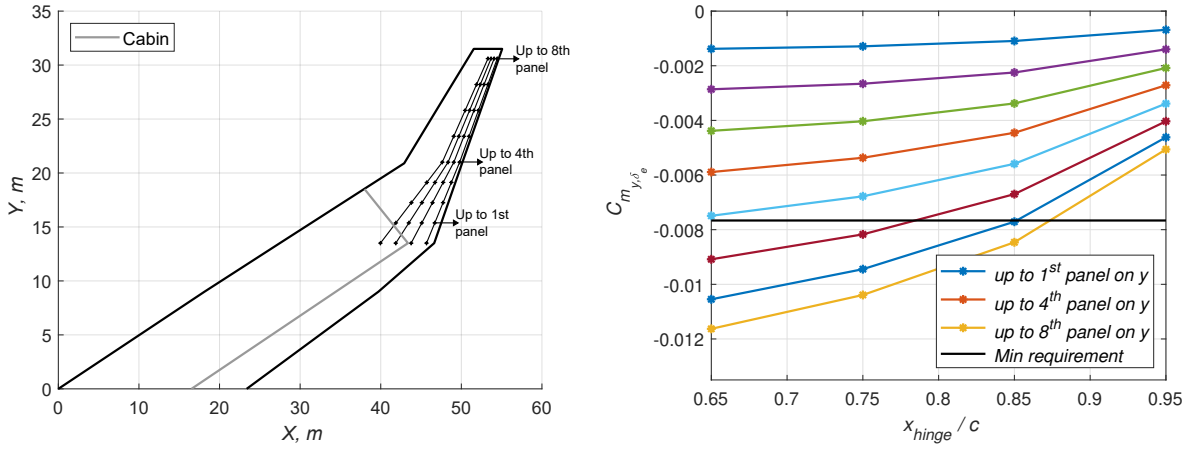

(a) Discretization of control surface in the aircraft trailing edge area

(b) Pitching moment control authority of the considered elevators and minimum control authority to satisfy the requirement

Fig. 5 Discretization of the elevator in the trailing edge area and corresponding pitching moment coefficient due to elevator

axis due to α and δ_e. The elevator considered here is the final one sized in this work. Figure 6b considered engine, as described in Section II.E.1. The results show that the thrust available is at least 8% higher than the thrust required.

α and T are the initial conditions for the remaining simulations and are kept constant through them. The center of gravity (CG) used in all the considered simulations is located at 28.1 m from the aircraft nose, corresponding to the most forward CG location considered for this aircraft. The combination of MTOW and the most forward CG location of the aircraft represents an extreme combination that would likely not occur in reality. For example, for the current aircraft, the weight at the most forward CG location is 61% of the MTOW, and the most forward CG at MTOW is 1 m more downstream than 28.1 m, as discussed in [9]. Hence, the combination of CG location and weight considered in this study allows one to size the elevator conservatively.

Figure 7a shows the deflection required by the selected elevator under different flight conditions. The minimum requirements in Figure 5b are calculated using VLM simulations. In Figure 7a, the obtained deflection angle is then scaled to take into account the Mach effect in VLM simulations, which leads to an increase in control authority with

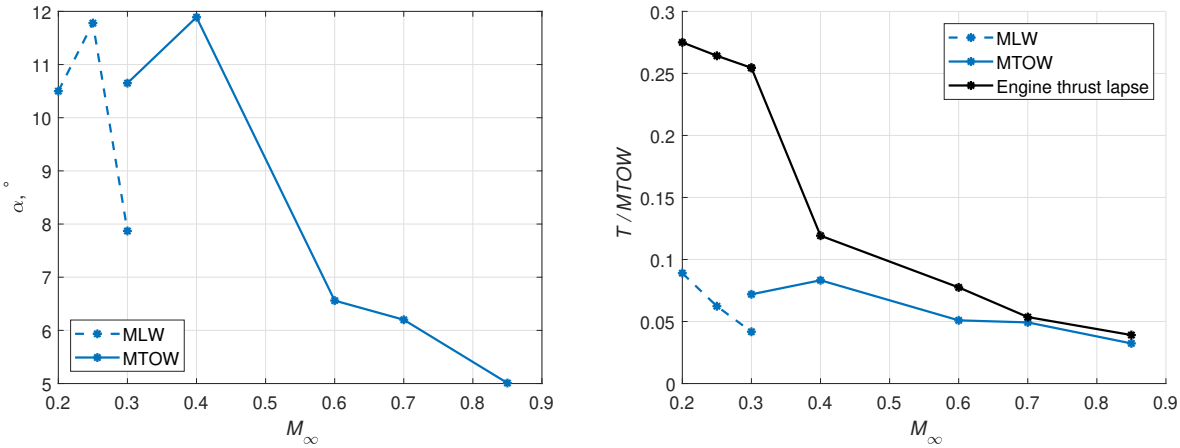

(a) Trim angle of attack

(b) Thrust to weight ratios

Fig. 6 Angle of attack and thrust required for longitudinal trim

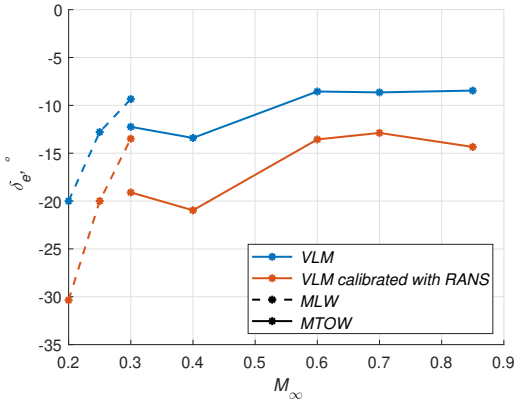

(a) Elevator trim deflection angles

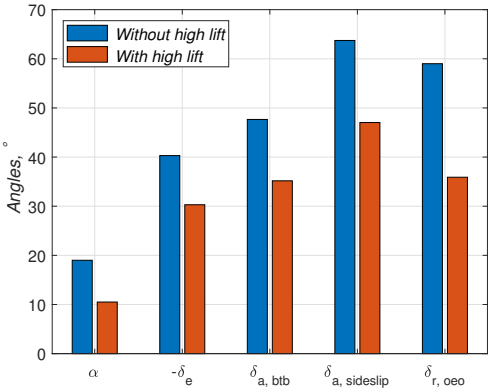

(b) Impact of high lift device on angle of attack and control surface deflections at $M_\infty = 0.2$

Fig. 7 Elevator deflections for longitudinal trim and impact of high lift device on other control surface requirements

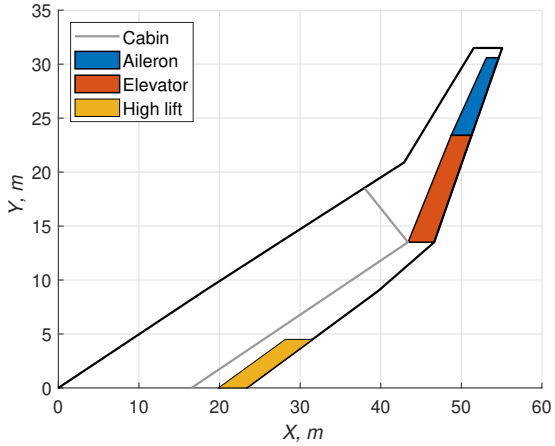

(a) Control surfaces on aircraft

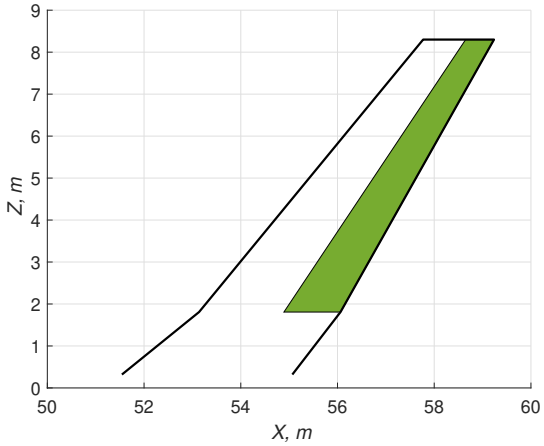

(b) Rudder on winglet

Fig. 8 Control surfaces identified in this study positioned on the aircraft

M_∞, so to a lower δ_e. Differently, when calibrating the VLM results with RANS simulations, the requirement in terms of deflection increases for all the considered conditions. VLM and RANS simulations are run for a fixed control surface at the different flight conditions, and the results obtained here in terms of deflection are then scaled to account for the difference. Additionally, the RANS are conducted at different α to account for the diminishing control authority of the control surfaces occurring at higher α. Further description of the simulations and results can be found in [9]. It should be noted that, as introduced in Section II.A, the forces and moments due to α and $\beta(\alpha)$ are always calculated with RANS simulations. Hence, if the aerodynamic model had been derived only with VLM simulations, the obtained deflections could have been even further from the VLM calibrated with RANS simulations. Overall, the elevator deflections predicted by VLM are between 31% and 41% lower than predicted by VLM calibrated with RANS simulations. The control surface that can provide the necessary control authority to serve as an elevator is depicted in Figure 8, together with the other control surfaces.

B. High lift devices

The results shown so far at $M_\infty = 0.2$ suppose the deployment of high lift devices. The reason for this choice is summarized in Figure 7b. The requirements in terms of control surface deflections decrease because of high lift device deployment. The high lift here considered leads to a reduction in the required deflections of 25% for the elevator and aileron, and 40% for the rudder.

Figure 8 depicts the high lift device employed. The surface is located inboard of the inner wing and near the CG to minimally impact the aircraft's pitching moment. The exact location of the surface along the span and, therefore, the extension along the chord can depend on the location of the engine, which is still under investigation [14]. The high lift surface has been simulated as a simple flap. However, because of the presence of the engine in the vicinity and to avoid interference with the flow at the engine inlet, the high lift device would realistically be installed on the lower side of the aircraft in the form of a split flap, which is actuated similarly to a spoiler. This configuration of the split flap has been tested experimentally in [16], proving the ability to significantly increase the lift with minimum impact on pitching moment.

As done previously, the VLM is calibrated with RANS simulations, leading to a deflection of 35°. The forces and moment generated by the high lift leads to a 8.5° angle of attack decrease. The high lift size and deployment have been selected to obtain $\delta_e < 35°$ for longitudinal trim and $\delta_a < 40°$ during bank-to-bank, which can still be critical based on the maximum aileron deflection employed in conventional aircraft. However, as seen in Figure 7b, at $M_\infty = 0.2$, the requirement for aileron to compensate the sideslip angle β is even higher than for the bank to bank maneuver.

If the high lift device cannot be implemented and the aircraft geometry is kept constant, the only parameter left to consider is the minimum speed at approach. For example, δ_e = -30° would be sufficient to trim the aircraft at M_∞ = 0.23 and U_∞ = 78.3 m/s. A smaller speed adjustment, for example, M_∞ = 0.22 and U_∞ = 73.9 m/s, could reduce the requirement of the high lift device considered here, leading to a deflection of 20° to obtain the same results as in Figure 7b, with the possibility of still having control authority to further reduce the requirements of the other control surfaces. For the continuation of the study, $M_\infty = 0.2$ is still considered as the minimum.

C. Sizing of Aileron and Rudder

The aileron is employed during the bank-to-bank maneuver but also to compensate for the effect of the sideslip angle and of the rudder when the aircraft faces the one engine inoperative condition. The deflections required from the aileron for the first two tested maneuvers are depicted in Figure 9a and 9b, respectively. The results for the one engine inoperative are not included for the aileron because the deflections are much lower than for the other cases, being at most $\delta_a = 2.1°$ for $M_\infty = 0.2$.

A procedure similar to elevator sizing (Section III.A) is used to size the aileron. The final aileron considered is depicted in Figure 8, where the aileron is located in the outer part of the aircraft.

For the elevator and aileron, the most critical condition occurs at $M_\infty = 0.2$ during the approach; for bank-to-bank maneuver, $\delta_a = 35°$. For the remaining cases, the requirement is at most 21.5° which is in line with the aileron deflection limits implemented in modern aircraft. Also, in this case, the deflections for the aileron predicted by the VLM are between 35% and 48% lower than the VLM calibrated with RANS. The results of Figure 9b, i.e., the aileron deflection required during sideslip, show how the presence of the large winglet is needed for accommodating the rudder on the winglets, hence on the further points from the CG, has a high impact on the aileron, leading to deflections that are sometimes higher than the bank-to-bank case, which should be the most critical for this type of actuator.

Before proceeding, it should be noticed that the sideslip requirements vary with flight conditions as described in Section II.E.2. In particular, the maximum value of β decreases with increasing freestream velocity and, therefore, with M_∞. However, the requirements for rudder deflections for the sideslip increase with M_∞ as depicted in Figure 10a. The reason for this trend is related to two main effects. First, at fixed α and β, the forces and moments induced on the aircraft increase with M_∞ however this effect is mainly compensated by the smaller requirement in terms of β at higher M_∞. The second effect is related to the difference in flow occurring in the aircraft before and after $M_\infty = 0.6$, hence when transonic effects occur. In subsonic cases, with fixed β, C_{m_z} acting on the aircraft decreases with α, which is in contrast to transonic conditions where the force and moment coefficients increase with α. For this reason, the transonic conditions are more critical in Figure 10a, and it should also be noted that the control authority of the considered control surfaces generally decreases with α. The effects here summarized are further discussed in [9], where the aerodynamic model used in this study is described in detail.

The rudder deflections in Figure 10a for $M_\infty \geq 0.6$ are at most 11°, which is lower than what an actuator mounted in modern airliners can achieve. As noted for the other control surfaces, VLM predicts between 43% and 53% lower

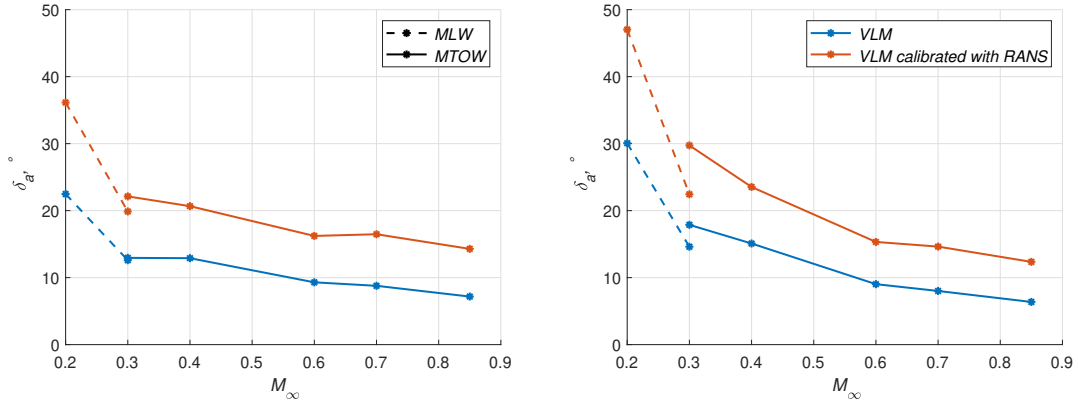

(a) Aileron deflection δ_a for bank-to-bank requirement

(b) Aileron deflection δ_a for sideslip

Fig. 9 Aileron deflections for bank-to-bank and sideslip requirements at different flight conditions

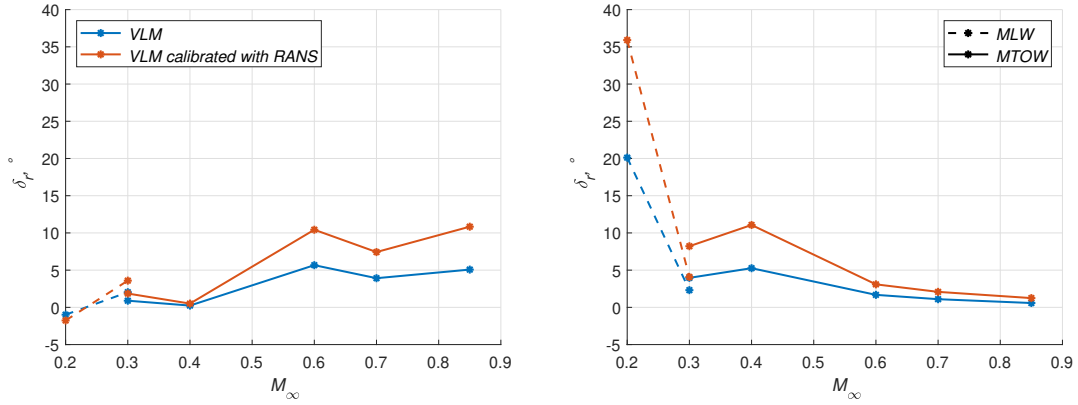

(a) Rudder deflection for sideslip requirement

(b) Rudder deflection for one engine inoperative requirement

Fig. 10 Rudder deflections for sideslip and one engine inoperative requirements at different flight conditions

deflections than VLM calibrated with RANS. It should be noted that the force and moment coefficients induced by $\beta(\alpha)$ are always determined with RANS simulations as introduced in Section II.A.

Figure 10b depicts the rudder deflections for the one engine requirement, showing higher requirements than for the sideslip cases at lower M_∞ and lower requirements at higher M_∞. Once again, the requirements at $M_\infty = 0.2$ are the highest and surpass the limits considered in Table 3.

Overall, these results show a different trend of the rudder with respect to the elevator and the aileron. For elevator and aileron, the requirements in terms of deflection angles tend to decrease with M_∞ and altitude. Conversely, the requirement for the rudder increases with M_∞ and altitude to satisfy the sideslip requirement, and it shows a similar trend as the other control surfaces for the one engine inoperative condition.

D. Verification of sizing - Coordinated Turn

In this last section, the coordinated turn is utilized as a verification maneuver to assess the final sizing of the control surfaces. As mentioned in Section II.F, executing this maneuver requires reaching and maintaining a bank angle ϕ between 40 and 45 degrees while keeping the sideslip angle β as close to zero as possible, with a flight path angle γ between 0 and 5 degrees. The maneuver is considered successful if these margins are satisfied for 10 seconds. Figure 11a shows the time history of the required angles. The angles are dimensionalized for ease of comparison, where $\beta^* = \beta/(max(\beta) - min(\beta))$, $\gamma^* = \gamma/max(\gamma)$ and $\phi^* = \phi/max(\phi)$. The max and min are the indicated margins above.

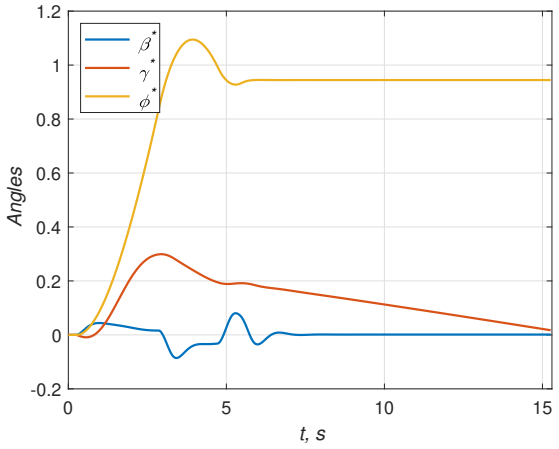

(a) Dimensionless angles during coordinated turn at M_∞ = 0.85

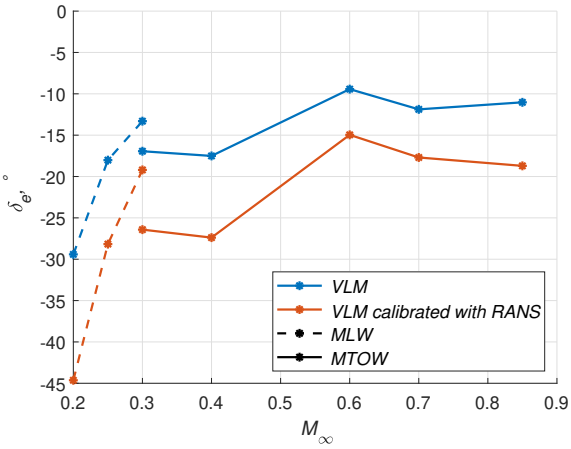

(b) Elevator deflection

Fig. 11 Angles evolution for coordinated turn and elevator deflection for coordinated turn at different operating conditions considered

Figure 11a shows, for M_∞ = 0.85, that with the layout of the selected control surfaces, it is possible to perform the coordinated turn within the limits defined by the certification documentation. Similar results are obtained in the other operating conditions considered in this study. The most demanding requirements are for the elevator, which are shown in Figure 11b. The required deflections are higher than the one for the longitudinal trim in Section III.A. In particular, as seen for all the cases so far, the highest δ_e are required at M_∞ = 0.2, leading to δ_e = -45°, which is relatively higher than the deflections that the conventional actuator can reach. However, in this study, the function of the elevator and aileron have been clearly divided. Still, it is always possible to use part or all the control surfaces considered as ailerons for trimming. Using an elevator as an aileron is not as straightforward if the deflection rate of the elevator is lower than that of the aileron as intended in this work. For example, the control surfaces in the trailing edge area, i.e., both elevator and aileron here sized, could be used to obtain the minimum trim drag at each operating condition as in [17]. During coordinated turn, at M_∞ = 0.7 and 0.85, the aircraft experiences α that are in the range for which $C_{m_{y,\alpha}} > 0$. The conditions under which this occurs are discussed in [9]. For simplicity in this work, during the coordinated turn at M_∞ = 0.7 and 0.85, $C_{m_{y,\alpha}} > 0$ is not considered.

IV. Conclusion

The present work proposed a control surface layout for a flying wing aircraft based on offline handling quality simulations. The simulations employed an aerodynamic model based on Reynolds-Averaged Navier-Stokes (RANS) and Vortex Lattice Method (VLM) simulations. The control authority of the elevator, aileron, and rudder is estimated both with VLM and VLM calibrated with RANS simulations.

Initial simulations have shown that the Dutch roll is stable for all flight conditions, resulting in Level 2 handling qualities based on MIL-STD-1797A. These results allowed simulations to be performed that would excite the aircraft simultaneously longitudinally and laterally without causing divergent behavior. Several simulations are then conducted to size each control surface. In particular, longitudinal trim for the elevator, steady heading sideslip, one engine inoperative for the rudder, and bank-to-bank for the aileron. Finally, coordinated turns are performed to verify whether the sized control surfaces could also comply with this requirement.

The simulations showed that it is possible to define a control surface layout that satisfies the certification requirements, with deflection rates similar to those of conventional aircraft and with elevator deflection δ_e < 30°, aileron deflection δ_a < 30° and rudder deflection δ_r < 35°. The only flight condition that does not always comply with the indicated deflections is approach landing weight with M_∞ = 0.2. To comply with the requirements at M_∞ = 0.2, a high lift device has been tested that shows the ability to reduce the requirement for the control surfaces greatly. However, in some cases, even further high lift deployment would be required to obtain deflections in line with the other operating conditions. Otherwise, a slight increase in the minimum speed would significantly reduce the requirement of the high lift device.

Simulations have been conducted to determine the control authority of control surfaces with VLM and VLM calibrated with RANS, showing that without RANS calibration, VLM would underestimate the requirement of control surfaces up to 50%.

Acknowledgments

This publication is part of the project Flying V Flight Control with project number 19511 of the research program Open Technology Programme, which is (partly) financed by the Dutch Research Council (NWO). The authors would like to acknowledge the in-kind contribution of KLM Royal Dutch Airlines and ADSE.

References

[1] Darecki, M., Edelstenne, C., Enders, T., et al., "Flightpath 2050 - Europe's Vision for Aviation," Tech. Rep. EUR 098 EN, European Commission, 2011.

[2] Bravo-Mosquera, P. D., Catalano, F. M., and Zingg, D. W., "Unconventional aircraft for civil aviation: A review of concepts and design methodologies," *Progress in Aerospace Sciences*, Vol. 131, 2022, pp. 1–29. https://doi.org/10.1016/j.paerosci.2022.100813.

[3] Benad, J., "The Flying V - A new aircraft configuration for commercial passenger transport," *Deutscher Luft-und Raumfahrtkongress*, Rostock, Germany, 2015. https://doi.org/10.25967/370094.

[4] Laar, Y., Atherstone, D., Benad, J., and Vos, R., "Aerodynamic Design of a Flying V Aircraft in Transonic Conditions," *AIAA SciTech*, Orlando, United States of America, January 2024. https://doi.org/10.2514/6.2024-2669.

[5] Atmaca, D., Stroosma, O., and van Kampen, E.-J., "Piloted Evaluation of Flying-V with Incremental Nonlinear Dynamic Inversion and Envelope Protection," *AIAA SciTech*, Orlando, United States of America, January 2025.

[6] EASA, "Acceptable Means of Compliance for Large Aeroplanes CS-25," Tech. Rep. Amendment 24, EASA, 2007.

[7] Denieul, Y., "Preliminary Design of Control Surfaces and Laws for Unconventional Aircraft Configurations," Ph.D. thesis, Institut Supérieur de l'Aéronautique et de l'Espace, 2016.

[8] Varriale, C., "Applying Control Allocation Methods to a Staggered Box-Wing Aircraft Configuration," Ph.D. thesis, Technische Universiteit Delft, 2022.

[9] Asaro, S., and Vos, R., "Synthesis of the Aerodynamic Model of a Flying Wing Aircraft," *AIAA SciTech*, Orlando, United States of America, January 2025.

[10] Oosterom, W., and Vos, R., "Conceptual Design of a Flying-V Aircraft Family," *AIAA SciTech*, Virtual event, January 2021. https://doi.org/10.2514/6.2022-3200.

[11] Hanke, C. R., and Nordwall, D. R., "The simulation of a jumbo jet transport aircraft. Volume 2: Modeling data," Tech. Rep. D6-30643, NASA, 1970.

[12] Matamoros, I., and de Visser, C. C., "Incremental Nonlinear Control Allocation for a Tailless Aircraft with Innovative Control Effectors," *2018 AIAA Guidance, Navigation, and Control Conference*, 2018. https://doi.org/10.2514/6.2018-1116.

[13] "Flying Qualities of Piloted Aircraft," Tech. rep., United States of America, Department of Defense, 1990.

[14] Kumar, A., Asaro, S., and Vos, R., "Aerodynamic Analysis of the Flying V Subsonic Transport to Enable Engine Integration," *AIAA SciTech*, Orlando, United States of America, 2025.

[15] Mattingly, J. D., Heiser, W. H., Boyer, K. M., Haven, B. A., and Pratt, D. T., *Aircraft Engine Design*, American Institute of Aeronautics and Astronautics, 2018.

[16] Eftekhar, S., "High Lift Split Flaps for the Flying-V," Master thesis, Technische Universiteit Delft, 2024.

[17] Woldhuis, T., Asaro, S., and Wang, X., "Online Data-Driven Optimization of Aerodynamic Performance for an Unconventional Morphing Aircraft," *AIAA SciTech*, Orlando, United States of America, January 2025.